ELSEVIER

Tight frame: an efficient way for high-resolution image reconstruction

Raymond H. Chan,[a,1] Sherman D. Riemenschneider,[b,*,2]
Lixin Shen,[b,3] and Zuowei Shen [c,4]

[a] *Department of Mathematics, the Chinese University of Hong Kong, Shatin, NT, PR China*
[b] *Department of Mathematics, Armstrong Hall, P.O. Box 6310, West Virginia University, Morgantown, WV 26505, USA*
[c] *Department of Mathematics, National University of Singapore, Science Drive 2, Singapore 117543, Singapore*

Abstract

High-resolution image reconstruction arise in many applications, such as remote sensing, surveillance, and medical imaging. The model proposed by Bose and Boo [Int. J. Imaging Syst. Technol. 9 (1998) 294–304] can be viewed as passing the high-resolution image through a blurring kernel, which is the tensor product of a univariate low-pass filter of the form $[1/2 + \varepsilon, 1, \ldots, 1, 1/2 - \varepsilon]$, where ε is the displacement error. Using a wavelet approach, bi-orthogonal wavelet systems from this low-pass filter were constructed in [R. Chan et al., SIAM J. Sci. Comput. 24 (4) (2003) 1408–1432; R. Chan et al., Linear Algebra Appl. 366 (2003) 139–155] to build an algorithm. The algorithm is very efficient for the case without displacement errors, i.e., when all $\varepsilon = 0$. However, there are several drawbacks when some $\varepsilon \neq 0$. First, the scaling function associated with the dual low-pass filter has low regularity. Second, only periodic boundary conditions can be imposed, and third, the wavelet filters so constructed change when some ε change. In this paper, we design tight-frame symmetric wavelet filters by using the unitary extension principle of [A. Ron, Z. Shen, J. Funct. Anal. 148 (1997) 408–447]. The wavelet filters do not depend on ε, and hence our algorithm essentially reduces to that of the case where $\varepsilon = 0$. This greatly simplifies the algorithm and resolves the drawbacks of the bi-orthogonal approach.

* Corresponding author.
  E-mail addresses: sherm@math.wvu.edu (S.D. Riemenschneider), lshen@math.wvu.edu (L. Shen).

1. Introduction

High-resolution images are often indispensable in many applications, such as remote sensing, surveillance, and medical imaging. Their reconstruction techniques can improve the resolution of image-acquisition systems like the CCD imaging sensor arrays. The reconstruction of high-resolution images from multiple low-resolution image frames can be modeled by

$$g = Hf + \eta, \tag{1}$$

where f is the desired high-resolution image, H is the blurring kernel, g is the observed high-resolution image formed from the low-resolution images, and η is the noise.

The system (1) is ill-posed. Usually it is solved by Tikhonov's regularization method. The Tikhonov-regularized solution is defined to be the unique minimizer of

$$\min_f \{ \|Hf - g\|^2 + \alpha R(f) \}, \tag{2}$$

where $R(f)$ is a regularization functional. The basic idea of regularization is to replace the original ill-posed problem with a "nearby" well-posed problem, whose solution approximates the required solution. The regularization parameter α provides a tradeoff between fidelity to the measurements and noise sensitivity.

Much research has been done in the last three decades on the high-resolution image reconstruction [8–10,12,15,17,18,20]. The model proposed by Bose and Boo in [1] is one of the mathematical models for reconstructing a high-resolution image from multiple low-resolution, shifted, degraded samples of a true scene. The model was solved in [1,15,16] using the least-squares approach in (2). Recently, we studied it from the wavelet point of view [2,3]. The main idea is to view the blurring kernel H as a matrix representation of a low-pass filter that gives a stable refinable function associated with a multiresolution of $\mathcal{L}^2(\mathbb{R}^2)$. Then the wavelet-based high-resolution image reconstruction procedure is essentially to approximate iteratively the wavelet coefficients folded by the given low-pass filter. The algorithms are developed through the perfect reconstruction formula of a bi-orthogonal wavelet system with this low-pass filter as its primary low-pass filter, see [2,3,21]. By incorporating the wavelet analysis viewpoint, many available techniques developed in the wavelet literature, such as wavelet-based denoising scheme, can be applied to this problem.

However, there are several difficulties when using the wavelet approach for problems with displacement errors:

(i) As is shown in [2], the high-resolution image is represented in the multiresolution generated by the dual low-pass filter. The corresponding scaling function normally has low regularity, and it affects the performance of the algorithm. To improve the regularity, one has to use longer dual filters. However, this increases the complexity of the computation and amplifies the artifacts around the boundary.

(ii) In image restoration, symmetric boundary conditions usually provide better results, see, for instance, [16]. For the algorithm in [3], the low-pass and the high-pass filters and their duals are no longer symmetric. This implies that symmetric boundary conditions cannot be imposed.

(iii) The construction of the dual filter depends on the displacement errors. This is particularly inconvenient when the errors vary with time in some applications such as the extraction of high-resolution images from video.

In this paper, we invoke the unitary extension principle of [19] to build a wavelet tight-frame system from the given low-pass filter. The constructed filters (both low and high) will be symmetric with self-duality. Hence, the symmetric boundary conditions can be imposed. Moreover, the recovered image is represented in the multiresolution derived from the given low-pass filter. This multiresolution is more natural and has the same regularity as the scaling function corresponding to the blurring filter. Furthermore, our analysis will show that the filter design is independent of the displacement errors. This leads to an algorithm that is independent of the displacement errors. Hence it can be adapted to a wider range of applications. Finally, the redundant nature of the tight-frame system can extract more features from the blurred images in the reconstruction of the high-resolution images.

We remark that the least-squares approach used in [1,15,16] also has difficulty when there are displacement errors. The blurring operator is no longer spatially invariant and hence the matrix does not have special structure. The Tikhonov system (2) has to be solved by an iterative method such as the preconditioned conjugate gradient method.

The outline of the paper is as follows. In Section 2, we introduce the model by Bose and Boo [1], and different boundary conditions. In Section 3, we recall the bi-orthogonal wavelet algorithm developed in [2,3]. In Section 4, we develop our tight-frame algorithm. Finally, numerical examples are given in Section 5 to illustrate the effectiveness of the algorithm.

For the rest of the paper, we will use the following notations. Bold-faced characters indicate vectors and matrices. The numbering of matrix and vector starts from 0. The matrix $\mathbf{L}^t$ denotes the transpose of the matrix $\mathbf{L}$. The symbols $\mathbf{I}$ and $\mathbf{0}$ denote the identity and zero matrices, respectively. For a given function $f \in \mathcal{L}^1(\mathbb{R})$, $\hat{f}(\omega) = \int_{\mathbb{R}} f(x)e^{-jx\omega}\,dx$ denotes the Fourier transform of f. For a given sequence m, $\hat{m}(\omega) = \sum_{k \in \mathbb{Z}} m(k)e^{-jk\omega}$ denotes the Fourier series of m, and $\hat{m}^*$ (or $\overline{\hat{m}}$) denotes the complex conjugate of $\hat{m}$. The Kronecker $\delta_{k,l} = 1$ if $k = l$ and 0 otherwise.

To describe Toeplitz, circulant, and Hankel matrices, we use the following notations:

$$\text{Toeplitz}(\mathbf{a}, \mathbf{b}) = \begin{pmatrix} a_0 & a_1 & \cdots & a_{N-2} & a_{N-1} \\ b_1 & a_0 & \cdots & a_{N-3} & a_{N-2} \\ \vdots & \vdots & \ddots & \vdots & \vdots \\ b_{N-2} & b_{N-3} & \cdots & a_0 & a_1 \\ b_{N-1} & b_{N-2} & \cdots & b_1 & a_0 \end{pmatrix} \quad \text{with } a_0 = b_0,$$

$$\text{Circulant}(\mathbf{a}) = \begin{pmatrix} a_0 & a_1 & \cdots & a_{N-2} & a_{N-1} \\ a_{N-1} & a_0 & \cdots & a_{N-3} & a_{N-2} \\ \vdots & \vdots & \ddots & \vdots & \vdots \\ a_2 & a_3 & \cdots & a_0 & a_1 \\ a_1 & a_2 & \cdots & a_{N-1} & a_0 \end{pmatrix},$$

and

$$\text{Hankel}(\mathbf{a}, \mathbf{b}) = \begin{pmatrix} a_0 & a_1 & \cdots & a_{N-2} & a_{N-1} \\ a_1 & a_2 & \cdots & a_{N-1} & b_{N-2} \\ \vdots & \vdots & \ddots & \vdots & \vdots \\ a_{N-2} & a_{N-1} & \cdots & b_2 & b_1 \\ a_{N-1} & b_{N-2} & \cdots & b_1 & b_0 \end{pmatrix} \quad \text{with } a_{N-1} = b_{N-1}.$$

The matrix pseudoHankel($\mathbf{a}, \mathbf{b}$) is formed from Hankel($\mathbf{a}, \mathbf{b}$) by replacing both the first column and the last column with zero vectors, i.e.,

$$\text{pseudoHankel}(\mathbf{a}, \mathbf{b}) = \begin{pmatrix} 0 & a_1 & \cdots & a_{N-2} & 0 \\ 0 & a_2 & \cdots & a_{N-1} & 0 \\ \vdots & \vdots & \ddots & \vdots & \vdots \\ 0 & a_{N-1} & \cdots & b_2 & 0 \\ 0 & b_{N-2} & \cdots & b_1 & 0 \end{pmatrix} \quad \text{with } a_{N-1} = b_{N-1}.$$

2. Mathematical model for high-resolution image reconstruction

In this section, we first introduce the mathematical model for high-resolution image reconstruction and then review three different boundary conditions used in the formulation of the blurring kernel.

2.1. Mathematical model

We follow the high-resolution reconstruction model proposed by Bose and Boo [1]. Consider a sensor array with $L \times L$ sensors in which each sensor has $N_1 \times N_2$ sensing elements and the size of each sensing element is $T_1 \times T_2$. For simplicity, L will be an even number in the following discussions. Our aim is to reconstruct an image with resolution $M_1 \times M_2$, where $M_1 = L \times N_1$ and $M_2 = L \times N_2$.

In order to have enough information to resolve the high-resolution image, there are subpixel displacements between the sensors in the sensor arrays. For sensor (ℓ_1, ℓ_2), $0 \leqslant \ell_1, \ell_2 < L$ with $(\ell_1, \ell_2) \neq (0, 0)$, its vertical and horizontal displacements $d^x_{\ell_1, \ell_2}$ and $d^y_{\ell_1, \ell_2}$ with respect to the $(0, 0)$th reference sensor are given by

$$d^x_{\ell_1, \ell_2} = \left(\ell_1 + \varepsilon^x_{\ell_1, \ell_2}\right)\frac{T_1}{L} \quad \text{and} \quad d^y_{\ell_1, \ell_2} = \left(\ell_2 + \varepsilon^y_{\ell_1, \ell_2}\right)\frac{T_2}{L}.$$

Here $\varepsilon^x_{\ell_1, \ell_2}$ and $\varepsilon^y_{\ell_1, \ell_2}$ are the vertical and horizontal *displacement errors*, respectively. They can be obtained by the manufacturers during camera calibration. Fig. 1 shows the case when we have a 2×2 sensor array. We assume that

$$\left|\varepsilon^x_{k_1, k_2}\right| < \frac{1}{2} \quad \text{and} \quad \left|\varepsilon^y_{k_1, k_2}\right| < \frac{1}{2}.$$
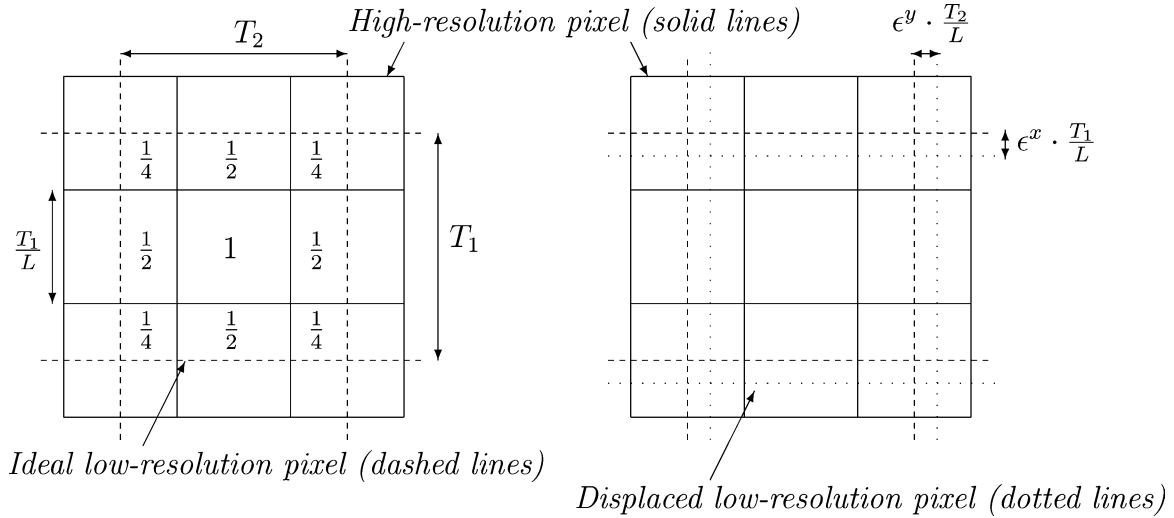
Fig. 1. Sensors without and with displacement error when $L = 2$ (left and right, respectively).

For sensor (ℓ_1, ℓ_2), the average intensity registered at its (n_1, n_2)th pixel is modeled by

$$g_{\ell_1,\ell_2}[n_1, n_2] = \frac{1}{T_1 T_2} \int_{T_1(n_1-1/2)+d^x_{\ell_1,\ell_2}}^{T_1(n_1+1/2)+d^x_{\ell_1,\ell_2}} \int_{T_2(n_2-1/2)+d^y_{\ell_1,\ell_2}}^{T_2(n_2+1/2)+d^y_{\ell_1,\ell_2}} f(x, y) \, dx \, dy + \eta_{\ell_1,\ell_2}[n_1, n_2]. \tag{3}$$

Here $0 \leqslant n_1 < N_1$ and $0 \leqslant n_2 < N_2$ and $\eta_{\ell_1,\ell_2}[n_1, n_2]$ is the noise, see [1]. We intersperse all the low-resolution images g_{ℓ_1,ℓ_2} to form an $M_1 \times M_2$ image g by assigning

$$g[Ln_1 + \ell_1, Ln_2 + \ell_2] = g_{\ell_1,\ell_2}[n_1, n_2].$$

The image g is already a high-resolution image and is called the *observed high-resolution image*. It is already a better image than any one of the low-resolution samples g_{ℓ_1,ℓ_2} themselves, c.f. the top two figures in Fig. 5.

To obtain an even better image than g (e.g., the bottom two figures in Fig. 5), one will have to find f from (3). One way is to discretize (3) using the rectangular quadrature rule and then solve the discrete system for f. Since the right-hand side of (3) involves the values of f outside the scene (i.e., outside the domain of g), the resulting system will have more unknowns than the number of equations, and one has to impose boundary conditions on f for points outside the scene, see, e.g., [1]. Then the blurring matrix corresponding to the (ℓ_1, ℓ_2)th sensor is given by a square matrix of the form

$$\mathbf{H}_{\ell_1,\ell_2}\big(\varepsilon^x_{\ell_1,\ell_2}, \varepsilon^y_{\ell_1,\ell_2}\big) = \mathbf{H}^y\big(\varepsilon^y_{\ell_1,\ell_2}\big) \otimes \mathbf{H}^x\big(\varepsilon^x_{\ell_1,\ell_2}\big). \tag{4}$$

The matrices $\mathbf{H}^x(\varepsilon^x_{\ell_1,\ell_2})$ and $\mathbf{H}^y(\varepsilon^y_{\ell_1,\ell_2})$ vary under different boundary conditions and will be given later.

The blurring matrix for the whole sensor array is made up of blurring matrices from each sensor

$$\mathbf{H}\big(\boldsymbol{\varepsilon}^x, \boldsymbol{\varepsilon}^y\big) = \sum_{\ell_1=0}^{L-1} \sum_{\ell_2=0}^{L-1} \mathbf{D}_{\ell_1,\ell_2} \mathbf{H}_{\ell_1,\ell_2}\big(\varepsilon^x_{\ell_1,\ell_2}, \varepsilon^y_{\ell_1,\ell_2}\big), \tag{5}$$

where $\boldsymbol{\varepsilon}^x = [\varepsilon^x_{\ell_1,\ell_2}]^{L-1}_{\ell_1,\ell_2=0}$ and $\boldsymbol{\varepsilon}^y = [\varepsilon^y_{\ell_1,\ell_2}]^{L-1}_{\ell_1,\ell_2=0}$. Here $\mathbf{D}_{\ell_1,\ell_2}$ is the sampling matrix for the (ℓ_1, ℓ_2)th sensor, and is given by

$$\mathbf{D}_{\ell_1,\ell_2} = \mathbf{D}_{\ell_2} \otimes \mathbf{D}_{\ell_1}, \tag{6}$$

where $\mathbf{D}_{\ell_j} = \mathbf{I}_{N_j} \otimes \mathbf{e}^t_{\ell_j}$ with $\mathbf{e}_{\ell_j}$ the jth unit vector.

Let $\mathbf{f}$ and $\mathbf{g}$ be the column vectors formed by f and g. The Tikhonov-regularization model in (2) becomes

$$\big(\mathbf{H}(\boldsymbol{\varepsilon}^x, \boldsymbol{\varepsilon}^y)^t \mathbf{H}(\boldsymbol{\varepsilon}^x, \boldsymbol{\varepsilon}^y) + \alpha \mathbf{R}\big)\mathbf{f} = \mathbf{H}(\boldsymbol{\varepsilon}^x, \boldsymbol{\varepsilon}^y)^t \mathbf{g}, \tag{7}$$

where $\mathbf{R}$ is the matrix corresponding to the regularization functional R in (2).

2.2. Boundary conditions

Here we consider three common boundary conditions used in image processing literatures, namely, the periodic, the half-point symmetric, and the whole-point symmetric conditions.

2.2.1. Periodic boundary condition

The periodic boundary condition assumes that

$$f(i \pm M_1, j \pm M_2) = f(i, j) \quad \text{for all } 0 \leqslant i < M_1,\ 0 \leqslant j < M_2.$$

The resulting $\mathbf{H}^x(\varepsilon^x_{\ell_1,\ell_2})$ and $\mathbf{H}^y(\varepsilon^y_{\ell_1,\ell_2})$ have a circulant structure:

$$\mathbf{H}^x(\varepsilon^x_{\ell_1,\ell_2}) = \frac{1}{L} \cdot \text{Circulant}(\mathbf{a}),$$

where

$$\mathbf{a} = \left[\overbrace{1, \ldots, 1}^{L/2\ \text{ones}},\, \frac{1}{2} - \varepsilon^x_{\ell_1,\ell_2}, 0, \ldots, 0, \frac{1}{2} + \varepsilon^x_{\ell_1,\ell_2},\, \overbrace{1, \ldots, 1}^{(L/2) - 1\ \text{ones}} \right]^t.$$

The matrix $\mathbf{H}^y(\varepsilon^y_{\ell_1,\ell_2})$ can be defined similarly. These matrices are circulant matrices.

When there are no displacement errors, i.e., when $\boldsymbol{\varepsilon}^x = \boldsymbol{\varepsilon}^y = \mathbf{0}$, then $\mathbf{H}^x(\varepsilon^x_{\ell_1,\ell_2}) = \mathbf{H}^x(0)$ and $\mathbf{H}^y(\varepsilon^x_{\ell_1,\ell_2}) = \mathbf{H}^y(0)$ for all $0 \leqslant \ell_1, \ell_2 < L$. Then (5) reduces to

$$\mathbf{H}(\mathbf{0}, \mathbf{0}) = \mathbf{H}^y(0) \otimes \mathbf{H}^x(0). \tag{8}$$

This matrix is a block–circulant–circulant–block (BCCB) matrix and can always be diagonalized by the discrete Fourier transform [1]. The resulting Tikhonov system (7) is a BCCB system, which can be inverted easily by fast Fourier transforms (FFT) provided that the matrix R is chosen suitably (e.g., identity matrix or Laplacian matrix with the same boundary condition).

However, when there are displacement errors, the blurring matrix $\mathbf{H}(\boldsymbol{\varepsilon}^x, \boldsymbol{\varepsilon}^y)$ is a nonsymmetric matrix with no special structure. The matrix has the same graph as $\mathbf{H}(\mathbf{0}, \mathbf{0})$, but the entries are no longer constant along the diagonals. Hence the matrix cannot be diagonalized by FFT. The Tikhonov system (7) can then be solved by an iterative method such as the preconditioned conjugate gradient method, see [1]. One possible choice of preconditioners is the matrix $\mathbf{H}(\mathbf{0}, \mathbf{0})$ in (8).

When compared to the symmetric boundary conditions that we are going to discuss next, the periodic boundary conditions usually give more prominent ringing effects at the boundary of the image unless the data is close to periodic; see [2,16].

2.2.2. Half-point symmetric boundary condition (Neumann boundary condition)

We assume that the image outside the scene is a reflection of that inside

$$
f(i, j) = f(p, q) \quad \text{for} \quad
\begin{cases}
p = -1 - i, & i < 0, \\
p = 2M_1 - 1 - i, & i > M_1 - 1, \\
q = -1 - j, & j < 0, \\
q = 2M_2 - 1 - j, & j > M_2 - 1.
\end{cases}
$$

The resulting $\mathbf{H}^x(\varepsilon^x_{\ell_1,\ell_2})$ and $\mathbf{H}^y(\varepsilon^y_{\ell_1,\ell_2})$ have a Toeplitz-plus-Hankel structure

$$
\mathbf{H}^x\big(\varepsilon^x_{\ell_1,\ell_2}\big) = \frac{1}{L} \cdot \text{Toeplitz}(\mathbf{a}, \mathbf{b}) + \frac{1}{L} \cdot \text{Hankel}(\mathbf{c}, \mathbf{d}),
$$

where

$$
\mathbf{a} = \left[\overbrace{1, \ldots, 1}^{L/2 \text{ ones}}, \frac{1}{2} - \varepsilon^x_{\ell_1,\ell_2}, 0, \ldots, 0 \right]^t, \qquad
\mathbf{b} = \left[\overbrace{1, \ldots, 1}^{L/2 \text{ ones}}, \frac{1}{2} + \varepsilon^x_{\ell_1,\ell_2}, 0, \ldots, 0 \right]^t \tag{9}
$$

and

$$
\mathbf{c} = \left[\overbrace{1, \ldots, 1}^{(L/2) - 1 \text{ ones}}, \frac{1}{2} + \varepsilon^x_{\ell_1,\ell_2}, 0, \ldots, 0 \right]^t, \qquad
\mathbf{d} = \left[\overbrace{1, \ldots, 1}^{(L/2) - 1 \text{ ones}}, \frac{1}{2} - \varepsilon^x_{\ell_1,\ell_2}, 0, \ldots, 0 \right]^t.
$$

The matrix $\mathbf{H}^y(\varepsilon^y_{\ell_1,\ell_2})$ can be defined similarly. These matrices are Toeplitz-plus-Hankel matrices.

When there are no displacement errors, then again $\mathbf{H}^x(\varepsilon^x_{\ell_1,\ell_2}) = \mathbf{H}^x(0)$ and $\mathbf{H}^y(\varepsilon^y_{\ell_1,\ell_2}) = \mathbf{H}^y(0)$ for all $0 \leqslant \ell_1, \ell_2 < L$. We thus have $\mathbf{H}(\mathbf{0}, \mathbf{0}) = \mathbf{H}^y(0) \otimes \mathbf{H}^x(0)$ again. This matrix is a block Toeplitz-plus-Hankel matrix with Toeplitz-plus-Hankel blocks. It can always be diagonalized by the discrete cosine transform [16]. When there are displacement errors, the blurring matrix $\mathbf{H}(\boldsymbol{\varepsilon}^x, \boldsymbol{\varepsilon}^y)$ is a nonsymmetric matrix with no special structure, and cannot be diagonalized by the discrete cosine transform. The Tikhonov system (7) can then be solved by the preconditioned conjugate gradient method with the corresponding $\mathbf{H}(\mathbf{0}, \mathbf{0})$ as a preconditioner; see [15,16].

Neumann boundary conditions have proved to be an effective model for high-resolution image reconstruction, both in terms of the computational cost and of minimizing the ringing effects near the boundary [16].

2.2.3. Whole-point symmetric boundary condition

Here we also assume reflection except for the pixels right at the boundary

$$
f(i, j) = f(p, q) \quad \text{for} \quad
\begin{cases}
p = -i, & i < 0, \\
p = 2M_1 - i, & i > M_1 - 1, \\
q = -j, & j < 0, \\
q = 2M_2 - j, & j > M_2 - 1.
\end{cases}
$$

The resulting $\mathbf{H}^x(\varepsilon^x_{\ell_1,\ell_2})$ and $\mathbf{H}^y(\varepsilon^y_{\ell_1,\ell_2})$ have a Toeplitz-plus-pseudoHankel structure

$$
\mathbf{H}^x\big(\varepsilon^x_{\ell_1,\ell_2}\big) = \frac{1}{L} \cdot \text{Toeplitz}(\mathbf{a}, \mathbf{b}) + \frac{1}{L} \cdot \text{pseudoHankel}(\mathbf{c}, \mathbf{d}),
$$

where **a** and **b** are given by (9), and

$$\mathbf{c} = \left[\overbrace{1,\ldots,1}^{L/2 \text{ ones}}, \frac{1}{2} + \varepsilon^x_{\ell_1,\ell_2}, 0, \ldots, 0 \right]^t \quad \text{and} \quad \mathbf{d} = \left[\overbrace{1,\ldots,1}^{L/2 \text{ ones}}, \frac{1}{2} - \varepsilon^x_{\ell_1,\ell_2}, 0, \ldots, 0 \right]^t.$$

The matrix $\mathbf{H}^y(\varepsilon^y_{\ell_1,\ell_2})$ can be defined similarly. This boundary condition is used in [2], where it produces good high-resolution images in terms of signal-to-noise ratio and of minimizing the ringing effects near the boundary.

3. Wavelet-based high-resolution image reconstruction

No matter which boundary condition is imposed on the model, the interior row of $\mathbf{H}^x(\varepsilon^x_{\ell_1,\ell_2})$ (similarly of $\mathbf{H}^y(\varepsilon^y_{\ell_1,\ell_2})$) is given by

$$\frac{1}{L} \left[0, \ldots, 0, \frac{1}{2} + \varepsilon^x_{\ell_1,\ell_2}, \overbrace{1,\ldots,1}^{L-1}, \frac{1}{2} - \varepsilon^x_{\ell_1,\ell_2}, 0, \ldots, 0 \right].$$

This motivated us in [2] and [3] to consider the blurring matrix $\mathbf{H}^y(\varepsilon^y_{\ell_1,\ell_2}) \otimes \mathbf{H}^x(\varepsilon^x_{\ell_1,\ell_2})$ as a low-pass filter acting on the image f. This low-pass filter is a tensor product of the univariate low-pass filter

$$\frac{1}{L} \left[\frac{1}{2} + \varepsilon, \overbrace{1,\ldots,1}^{L-1}, \frac{1}{2} - \varepsilon \right], \tag{10}$$

where the parameter ε may vary in the x and y directions for each sensor. Using this observation, a wavelet algorithm based on bi-orthogonal wavelet systems was proposed in [2] for spatially invariant blurring kernels and in [3] for spatially variant blurring kernels. A detailed review of this algorithm is given in this section since our new algorithm, based on the tight-frame wavelet system, is an improvement of this algorithm.

3.1. Bi-orthogonal wavelet systems

We start from a compactly supported scaling function ϕ and the corresponding multiresolution with dilation L. The scaling function ϕ satisfies a refinement equation

$$\phi(x) = L \sum_{k \in \mathbb{Z}} m_0(k) \phi(Lx - k) \tag{11}$$

and the normalization condition $\hat{\phi}(0) = 1$, where the finitely supported sequence m_0 is a refinement mask (low-pass filter) defined on $\mathbb{Z}$ that satisfies $\sum_{k \in \mathbb{Z}} m_0(k) = 1$.

For a given refinement mask m_0, the corresponding refinable function can be determined in terms of its Fourier transform. For example, let $_{L,\varepsilon}m_0$ be the filter given in (10), i.e.,

$$_{L,\varepsilon}m_0 = \frac{1}{L}\left[\frac{1}{2}+\varepsilon, \overbrace{1,\ldots,1}^{L-1}, \frac{1}{2}-\varepsilon\right]$$

with the index of the filter $_{L,\varepsilon}m_0$ starting from $-L/2$ to $L/2$. The Fourier transform of the corresponding scaling function $_{L,\varepsilon}\phi$ is

$$_{L,\varepsilon}\hat{\phi}(\omega) = \prod_{k=1}^{\infty} {_{L,\varepsilon}\hat{m}_0}\left(L^{-k}\omega\right),$$

where $_{L,\varepsilon}\hat{m}_0$ is the Fourier series of the sequence $_{L,\varepsilon}m_0$. It can be proven that $_{L,\varepsilon}\phi$ is stable, i.e., $\{\phi(\cdot - j):\ j \in \mathbb{Z}\}$ forms a Riesz basis of V_0, the closed shift invariant space generated by $\{\phi(\cdot - j):\ j \in \mathbb{Z}\}$. It is supported in $[-L/(2(L-1)), L/(2(L-1))] \subset [-1, 1]$. Moreover, it was shown in [21] that $_{L,\varepsilon}\phi$ is Hölder continuous with Hölder exponent

$$-\frac{\ln\max(|1/2+\varepsilon|, |1/2-\varepsilon|)}{\ln L}. \tag{12}$$

For a compactly supported stable scaling function $\phi \in \mathcal{L}^2(\mathbb{R})$, let V_0 be the closed shift-invariant space generated by $\{\phi(\cdot - j):\ j \in \mathbb{Z}\}$ and $V_n := \{f(L^n\cdot):\ f \in V_0, n \in \mathbb{Z}\}$. It is known that when $\phi \in \mathcal{L}^2(\mathbb{R})$ is a compactly supported scaling function, then $\{V_n\}$ forms a multiresolution. Recall that a multiresolution is a family of closed subspaces $\{V_n\}_{n\in\mathbb{Z}}$ of $\mathcal{L}^2(\mathbb{R})$ that satisfies:

(i) $V_n \subset V_{n+1}$,
(ii) $\bigcup_n V_n$ is dense in $\mathcal{L}^2(\mathbb{R})$, and
(iii) $\bigcap_n V_n = \{0\}$ (see [5,13]).

A stable function $\tilde{\phi} \in \mathcal{L}^2(\mathbb{R})$ is called a dual function of the stable $\phi \in \mathcal{L}^2(\mathbb{R})$ if

$$\int_{\mathbb{R}} \phi(x-k)\tilde{\phi}(x-k')\,dx = \delta_{k,k'} \quad \forall\, k, k' \in \mathbb{Z}.$$

Often we call ϕ and $\tilde{\phi}$ a dual pair.

To get bi-orthogonal wavelet systems from $_{L,\varepsilon}\phi$, one needs to construct its dual scaling function. This can be done using the method in [21]. This leads to two multiresolutions, $\{V_n\}$ and $\{\tilde{V}_n\}$, with the associated scaling functions $_{L,\varepsilon}\phi$ and $_{L,\varepsilon}\tilde{\phi}$ being a dual pair. It is well known that for a dual pair of scaling functions ϕ and $\tilde{\phi}$, their corresponding low-pass filters $\hat{m}_0$ and $\hat{\tilde{m}}_0$ satisfy

$$\sum_{t=0}^{L-1} \hat{m}_0(\xi + \vartheta_t)\hat{\tilde{m}}_0^{\,*}(\xi + \vartheta_t) = 1, \tag{13}$$

where $\vartheta_t = 2\pi t/L$, $t = 0, 1, \ldots, L-1$. The key step in obtaining the dual wavelet system from the two dual multiresolutions is to use the matrix extension results of [14,22]. For a given pair of dual

low-pass filters satisfying (13), the matrix extension method provides a way to construct $\hat{m}_s$ and $\hat{\tilde{m}}_s$, $s = 1, \ldots, L-1$, so that

$$\sum_{t=0}^{L-1} \hat{m}_s(\omega + \vartheta_t)\hat{\tilde{m}}_{s'}^*(\omega + \vartheta_t) = \delta_{s,s'}, \quad 0 \leqslant s, s' \leqslant L-1.$$

The functions ψ_s and $\tilde{\psi}_s$, $1 \leqslant s \leqslant L-1$, which are defined by

$$\hat{\psi}_s(\omega) = \hat{m}_s\left(\frac{\omega}{L}\right)\hat{\phi}\left(\frac{\omega}{L}\right) \quad \text{and} \quad \hat{\tilde{\psi}}_s(\omega) = \hat{\tilde{m}}_s\left(\frac{\omega}{L}\right)\hat{\tilde{\phi}}\left(\frac{\omega}{L}\right),$$

are multi-band bi-orthogonal wavelets constructed from the multiresolution $\{V_n\}$ and $\tilde{V}_n$. The Fourier coefficient sequences of $\hat{m}_s$ and $\hat{\tilde{m}}_s$, $1 \leqslant s \leqslant L-1$, are called wavelet masks or high-pass filters. A complete analysis of bi-orthogonal wavelets can be found in [4].

   The wavelet-based algorithms in [2,3] are based on the existence of a bi-orthogonal wavelet system with $_{L,\varepsilon}m_0$ as one of the low-pass filters. Specifically, the bi-orthogonal wavelet system with $_{L,\varepsilon}m_0$ as one of the low-pass filters of the associated analysis was constructed and used in [2,3] for the cases $L = 2$ and 4. For arbitrary L, the minimally supported bi-orthogonal wavelet system with $_{L,\varepsilon}m_0$ as one of the low-pass filters is given explicitly in [21].

3.2. Image reconstruction algorithm

   Here, we briefly discuss the wavelet approach developed in [2,3]. Let $\{_{L,\varepsilon}m_s, {}_{L,\varepsilon}\tilde{m}_s\}_{s=0}^{L-1}$ be the bi-orthogonal filter banks corresponding to a pair of dual scaling functions $_{L,\varepsilon}\phi$ and $_{L,\varepsilon}\tilde{\phi}$ and dual wavelets $_{L,\varepsilon}\psi_s$ and $_{L,\varepsilon}\tilde{\psi}$. Then, they satisfy the perfect reconstruction equation

$$\sum_{s=0}^{L-1} {}_{L,\varepsilon}\hat{m}_s(\omega) \, {}_{L,\varepsilon}\hat{\tilde{m}}_s^*(\omega) = 1. \tag{14}$$

This equation is the starting point of our wavelet-based algorithm for high-resolution image reconstruction. For the (ℓ_1, ℓ_2)th sensor, the matrix representation of the perfect reconstruction of the bi-orthogonal system (14) in the x-direction is

$$\sum_{s=0}^{L-1} \tilde{\mathbf{M}}_s^x\big(\varepsilon_{\ell_1,\ell_2}^x\big)^{\text{t}} \mathbf{M}_s^x\big(\varepsilon_{\ell_1,\ell_2}^x\big) = \mathbf{I}_{M_1}, \tag{15}$$

where $\mathbf{M}_s^x(\varepsilon_{\ell_1,\ell_2}^x)$ and $\tilde{\mathbf{M}}_s^x(\varepsilon_{\ell_1,\ell_2}^x)$, $0 \leqslant s \leqslant L$, are the matrix representations of the primary filter $_{L,\varepsilon}m_s$ and the dual filter $_{L,\varepsilon}\tilde{m}_s$, respectively. Similar, in the y-direction, we have

$$\sum_{s=0}^{L-1} \tilde{\mathbf{M}}_s^y\big(\varepsilon_{\ell_1,\ell_2}^y\big)^{\text{t}} \mathbf{M}_s^y\big(\varepsilon_{\ell_1,\ell_2}^y\big) = \mathbf{I}_{M_2}. \tag{16}$$

   We have two remarks about (15) and (16):

(i) For $s = 0$, $\mathbf{M}_0^x(\varepsilon_{\ell_1,\ell_2}^x) = \mathbf{H}^x(\varepsilon_{\ell_1,\ell_2}^x)$ and $\mathbf{M}_0^y(\varepsilon_{\ell_1,\ell_2}^y) = \mathbf{H}^y(\varepsilon_{\ell_1,\ell_2}^y)$, i.e., $\mathbf{M}_0^y(\varepsilon_{\ell_1,\ell_2}^y) \otimes \mathbf{M}_0^x(\varepsilon_{\ell_1,\ell_2}^x) = \mathbf{H}_{\ell_1,\ell_2}(\varepsilon_{\ell_1,\ell_2}^x, \varepsilon_{\ell_1,\ell_2}^y)$, the blurring matrices for each sensor as given in (4).

(ii) If we impose the periodic boundary condition, then (15) and (16) both hold for any displacement errors including the case $\boldsymbol{\varepsilon}^x = \boldsymbol{\varepsilon}^y = \mathbf{0}$. However, if we impose the whole-point symmetric boundary condition, then (15) and (16) hold only when $\boldsymbol{\varepsilon}^x = \boldsymbol{\varepsilon}^y = \mathbf{0}$. This is one of the shortcomings of the bi-orthogonal wavelet method, as symmetric boundary conditions usually give better performance than periodic boundary conditions.

When (15) and (16) both hold, then for the (ℓ_1, ℓ_2)th sensor, we have

$$\sum_{p,q=0}^{L-1} \tilde{\mathbf{M}}_{p,q}\left(\varepsilon_{\ell_1,\ell_2}^x, \varepsilon_{\ell_1,\ell_2}^y\right)^{\mathrm{t}} \mathbf{M}_{p,q}\left(\varepsilon_{\ell_1,\ell_2}^x, \varepsilon_{\ell_1,\ell_2}^y\right) = \mathbf{I}_{M_1 \times M_2}, \tag{17}$$

where

$$\mathbf{M}_{p,q}\left(\varepsilon_{\ell_1,\ell_2}^x, \varepsilon_{\ell_1,\ell_2}^y\right) = \mathbf{M}_q^y\left(\varepsilon_{\ell_1,\ell_2}^y\right) \otimes \mathbf{M}_p^x\left(\varepsilon_{\ell_1,\ell_2}^x\right)$$

and

$$\tilde{\mathbf{M}}_{p,q}\left(\varepsilon_{\ell_1,\ell_2}^x, \varepsilon_{\ell_1,\ell_2}^y\right) = \tilde{\mathbf{M}}_q^y\left(\varepsilon_{\ell_1,\ell_2}^y\right) \otimes \tilde{\mathbf{M}}_p^x\left(\varepsilon_{\ell_1,\ell_2}^x\right).$$

In particular, by the first remark above, $\mathbf{M}_{0,0}(\varepsilon_{\ell_1,\ell_2}^x, \varepsilon_{\ell_1,\ell_2}^y) = \mathbf{H}_{\ell_1,\ell_2}(\varepsilon_{\ell_1,\ell_2}^x, \varepsilon_{\ell_1,\ell_2}^y)$.

In order to introduce the wavelet-based high-resolution image reconstruction algorithm, we first consider the case without displacement errors. (In this case, both periodic and whole-point symmetric boundary conditions can be applied.) Then (17) holds for every sensor. For simplicity, in this case we rewrite (17) as

$$\sum_{p,q=0}^{L-1} \tilde{\mathbf{M}}_{p,q}^{\mathrm{t}} \mathbf{M}_{p,q} = \mathbf{I}_{M_1 \times M_2}, \tag{18}$$

where $\mathbf{M}_{0,0} = \mathbf{H}(\mathbf{0}, \mathbf{0})$, the blurring matrix for the whole sensor array. Multiplying both sides of (18) by $\mathbf{f}$, we have

$$\sum_{p,q=0}^{L-1} \tilde{\mathbf{M}}_{p,q}^{\mathrm{t}} \mathbf{M}_{p,q} \mathbf{f} = \mathbf{f}.$$

Since $\mathbf{M}_{0,0}\mathbf{f} = \mathbf{H}(\mathbf{0}, \mathbf{0})\mathbf{f} = \mathbf{g}$ is just the observed high-resolution image, and the other $\mathbf{M}_{p,q}\mathbf{f}$, $(p, q) \neq (0, 0)$, represent the high-frequency components of $\mathbf{f}$, we obtain an iterative algorithm

$$\mathbf{f}_{n+1} = \tilde{\mathbf{M}}_{0,0}^{\mathrm{t}} \mathbf{g} + \sum_{\substack{p,q=0 \\ (p,q)\neq(0,0)}}^{L-1} \tilde{\mathbf{M}}_{p,q}^{\mathrm{t}} \mathbf{M}_{p,q} \mathbf{f}_n. \tag{19}$$

A complete analysis of this algorithm in terms of multiresolution was given in [2]. In fact, it was pointed out in [2] that the first term in the right-hand side of (19) is the representation of the observed image in the higher resolution subspace in the multiresolution generated by the dual low-pass filter of the given low-pass filter. Reconstructing the high-resolution image $\mathbf{f}$ is equivalent to recovering the wavelet coefficients of the original image $\mathbf{f}$, which are not available. In the algorithm, the wavelets coefficients of $\mathbf{f}$ are approximated by those of the previous iterate $\mathbf{f}_n$ (expressed by the rest of the terms in the right-hand side of (19)).

Further, a nonlinear denoising scheme can be built into (19) to remove the noise. This leads to the following algorithm:

$$\mathbf{f}_{n+1} = \tilde{\mathbf{M}}_{0,0}^{t}\mathbf{g} + \sum_{\substack{p,q=0 \\ (p,q)\neq(0,0)}}^{L-1} \tilde{\mathbf{M}}_{p,q}^{t}\mathcal{D}(\mathbf{M}_{p,q}\mathbf{f}_n).$$

Here $\mathcal{D}$ is a nonlinear denoising operator and we will discuss it in more detail later, see (38). The algorithm is generalized to the case with displacement errors in [3]. In this case, as mentioned by remark (ii), we can only impose periodic boundary conditions.

4. Tight frame for high-resolution image reconstruction

The wavelet approach puts the high-resolution image reconstruction into the multiresolution framework and provides us with a new way of understanding high-resolution image reconstruction. The numerical simulations show a significant improvement compared with the least-squares method. However, as seen in the last section on the description of the algorithms in [2,3], there are three major issues with the wavelet approach when applied to the case with displacement errors.

 (i) Since the image is represented in the multiresolution generated by the dual low-pass filter (see [2,3, 21]), the regularity of the dual refinable function plays a key role on the performance of the wavelet-based algorithm. However, the regularity of the refinable functions varies with the displacement errors, and in some cases, the function can even be discontinuous [21]. Although the regularity can be improved by increasing the length of the dual low-pass filter $_{L,\varepsilon}\tilde{m}_0$, it would produce ringing effects and increase the computational complexity.
 (ii) Since the filters are not symmetric, we only can impose the periodic boundary conditions. However, numerical results from both the least squares and the wavelet methods for problems with no displacement errors show that the symmetric boundary conditions usually provide much better performance than periodic boundary conditions, see, for instance, [2,3,16].
(iii) The design of the filters depends on the displacement errors. This restricts the usage of our method for applications where the displacement errors vary with time and need to be estimated continuously. One such example is the extraction of high-resolution images from video where the displacement errors vary continuously and are estimated numerically.

In this paper, we resolve these issues by using tight-frame systems. To design a tight frame that can solve the problems, we resort to analyzing the properties of the filter $_{L,\varepsilon}m_0$. The motivation comes from the splitting of the low-pass filter as follows:

$$_{L,\varepsilon}m_0 = \frac{1}{L}\left[\frac{1}{2}+\varepsilon, \overbrace{1,\ldots,1}^{L-1}, \frac{1}{2}-\varepsilon\right] = \frac{1}{L}\left[\frac{1}{2}, \overbrace{1,\ldots,1}^{L-1}, \frac{1}{2}\right] + (\sqrt{2}\varepsilon)\cdot\frac{\sqrt{2}}{2L}\left[1, \overbrace{0,\ldots,0}^{L-1}, -1\right]$$

$$= {}_{L,0}m_0 + (\sqrt{2}\varepsilon)\,_{L,0}m_1, \tag{20}$$

where

$$_{L,0}m_0 = \frac{1}{L}\left[\frac{1}{2}, \overbrace{1,\ldots,1}^{L-1}, \frac{1}{2}\right] \quad \text{and} \quad _{L,0}m_1 = \frac{\sqrt{2}}{2L}\left[1, \overbrace{0,\ldots,0}^{L-1}, -1\right].$$

Let the Fourier series of the filters $_{L,0}m_0$ and $_{L,0}m_1$ be denoted by $_L\tau_0$ and $_L\tau_1$, respectively. Observation (20) is crucial in this paper, since all we need now is to *construct a tight-frame system with* $_L\tau_0$ *as its low-pass filter and* $_L\tau_1$ *as one of its high-pass filters.* Since $_L\tau_0$ and $_L\tau_1$ are symmetric and independent of ε, we can expect the filters in the tight-frame systems to be symmetric and independent of ε. We will also see that $_L\tau_1$ will "collect" the displacement errors at each iterate. Hence, the algorithm is essentially reduced to the case with no displacement errors. This also means that the reconstructed image is represented in the multiresolution generated by the blurring low-pass filter with no displacement errors. As seen in (12), the scaling function generated by the blurring filter with no displacement errors has higher regularity than those generated by the blurring filters with displacement errors. Altogether, this provides solutions to the problems mentioned above.

4.1. Wavelet tight frame and filter design

At first look, it seems difficult to design wavelet systems with one pre-given low-pass filter and one pre-given high-pass filter especially when L is large. Here, we give an explicit construction of this tight frame by exploiting the specific structure of the filters $_L\tau_0$ and $_L\tau_1$ using the unitary extension principle of [19].

Given a finite set $\Psi \subset \mathcal{L}^2(\mathbb{R})$, the *wavelet system* generated by Ψ is defined as

$$X = \left\{L^{k/2}\psi\left(L^k \cdot -j\right)\colon \psi \in \Psi, \ k, j \in \mathbb{Z}\right\}. \tag{21}$$

A system $X \subset \mathcal{L}^2(\mathbb{R})$ with countably many elements is a *tight frame* if for all $f \in \mathcal{L}^2(\mathbb{R})$,

$$\|f\|^2 = \sum_{g \in X}\left|\langle f, g\rangle\right|^2.$$

In particularly, an orthonormal basis is a tight frame. To use the unitary extension principle [19], we start with a compactly supported scaling function $\phi \in \mathcal{L}^2(\mathbb{R})$ with refinement mask (low-pass filter) τ_ϕ in (11) and its associated multiresolution V_n, $n \in \mathbb{Z}$.

For a given compactly supported refinable function in $\mathcal{L}^2(\mathbb{R})$, the construction of tight-frame wavelet systems is to find a finite set Ψ in V_1 such that the wavelet system generated by Ψ as defined in (21) forms a tight frame of $\mathcal{L}^2(\mathbb{R})$. Recall that an arbitrary $\psi \in V_1$ can be represented in the Fourier domain as

$$\hat{\psi}(L\cdot) = \tau_\psi\hat{\phi}$$

for some 2π-periodic τ_ψ (see, e.g., [19]). The unitary extension principle in [19] says that the wavelet system forms a tight frame in $\mathcal{L}^2(\mathbb{R})$ provided that τ_ϕ together with τ_ψ, $\psi \in \Psi$, satisfy the following conditions:

$$\tau_\phi(\omega)\overline{\tau_\phi(\omega + \vartheta_p)} + \sum_{\psi \in \Psi}\tau_\psi(\omega)\overline{\tau_\psi(\omega + \vartheta_p)} = \delta_{p,0}, \tag{22}$$

where $\vartheta_p = 2\pi p/L$, $0 \leqslant p < L$. The sequences of the Fourier coefficients of τ_ψ, as well as τ_ψ itself, are called wavelet masks or high-pass filters.

Now let us return to our problem. We want to design a tight-frame system with $_L\tau_\phi = {_L\tau_0}$ as its low-pass filter and $_L\tau_1$ as one of its high-pass filters. The first question is the existence of such filters satisfying (22). To answer this question, let us look at the case when $L = 2$. In this case, we do have a tight-frame system with filters:

$$_2m_0 = \frac{1}{2}\left[\frac{1}{2}, 1, \frac{1}{2}\right], \quad _2m_1 = \frac{\sqrt{2}}{4}[1, 0, -1], \quad \text{and} \quad _2m_2 = \frac{1}{2}\left[-\frac{1}{2}, 1, -\frac{1}{2}\right]. \tag{23}$$

Let $_2\tau_0$, $_2\tau_1$, and $_2\tau_2$ be the corresponding Fourier series of the above filters. They satisfy

$$_2\tau_0(\omega)\overline{_2\tau_0(\omega + \ell\pi)} + {_2\tau_1(\omega)}\overline{_2\tau_1(\omega + \ell\pi)} + {_2\tau_2(\omega)}\overline{_2\tau_2(\omega + \ell\pi)} = \delta_{\ell,0}, \quad \ell = 0, 1. \tag{24}$$

Hence, it leads to a tight-frame system. In fact, this system is the first example given in a systematic construction of spline tight-frame wavelet systems by applying the unitary extension principle in [19].

Based on the tight-frame system for $L = 2$, we can design tight-frame systems for any $L = 2K$, where K is a positive integer. We note that $_L\tau_0$ and $_L\tau_1$ can be written in the Fourier domain as

$$_L\tau_0(\omega) = {_K\hat{h}_0(2\omega)} {_2\tau_0(\omega)} \quad \text{and} \quad _L\tau_1(\omega) = {_K\hat{h}_0(2\omega)} {_2\tau_1(\omega)},$$

where $_Kh_0 = (1/K)[1, \ldots, 1]$. The filter $_Kh_0$ is the refinement mask of the characteristic function on interval $[0, 1]$ with the dilation K. The scaling functions corresponding to the low-pass filters $_2\tau_0$, $_4\tau_0$, and $_6\tau_0$ are shown in Fig. 2.

There are several ways to construct wavelet masks satisfying (22). We choose the filters $_Kh_k$, which are related to the DCT III matrix of order K
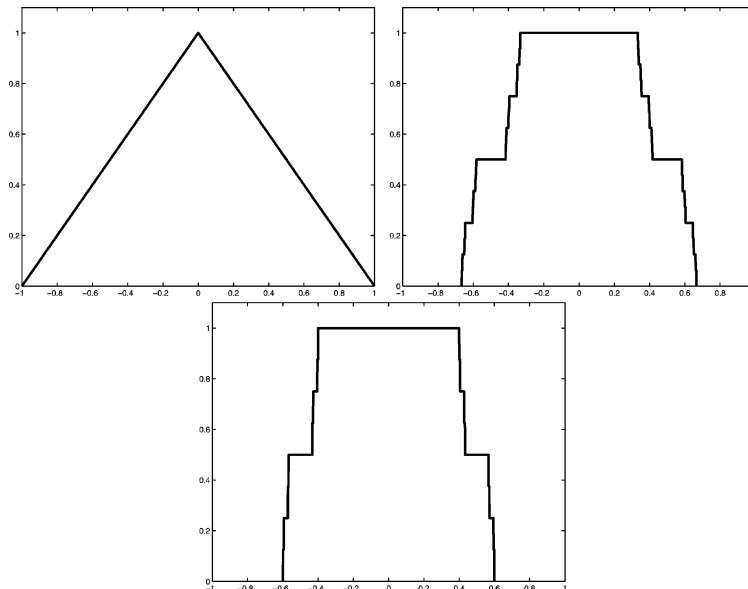
$$_Kh_0 = \frac{1}{K}[1, 1, \ldots, 1],$$

Fig. 2. Scaling functions (from left to right) with $_2\tau_0$, $_4\tau_0$, and $_6\tau_0$ as its low-pass filter, respectively.

$$_K h_k = \frac{\sqrt{2}}{K}\left[\cos\left(\frac{k\pi}{2K}\right), \cos\left(\frac{3k\pi}{2K}\right), \ldots, \cos\left(\frac{(2K-1)k\pi}{2K}\right)\right], \quad 0 \leqslant k \leqslant K-1.$$

Since $\cos((2\ell+1)k\pi)/(2K) = (-1)^k \cos((2(K-\ell)-1)k\pi)/(2K)$ for all $0 \leqslant \ell < K$, the filter $_K h_k$ (and hence the filter $_L \tau_k$) is symmetric for even k and antisymmetric for odd k. Let $_K \hat{h}_k$, $0 \leqslant k \leqslant K-1$, be the Fourier series of the above filter, then it can be proven (see [11]) that $_K \hat{h}_k$, $0 \leqslant k \leqslant K-1$, satisfy (22), i.e.,

$$\sum_{q=0}^{K-1} {}_K\hat{h}_q(2\omega) \, \overline{_K\hat{h}_q\left(2\omega + \frac{2\pi\ell}{K}\right)} = \delta_{\ell,0}, \quad 0 \leqslant \ell \leqslant K-1. \tag{25}$$

It is, in fact, an orthonormal Haar wavelet corresponding to the multiresolution generated by the characteristic function of the unit interval with dilation K. In general, we define

$$_L\tau_{3p+q}(\omega) = {}_K\hat{h}_p(2\omega)\, _2\tau_q(\omega), \quad q = 0, 1, 2, \text{ and } 0 \leqslant p \leqslant K-1. \tag{26}$$

Therefore, we get a tight-frame system derived from a multiresolution generated by the blurring low-pass filter $_L\tau_0$ with the high-pass filter $_L\tau_1$ as one of the wavelet masks once we proved that they satisfy (22). This is proven in the next theorem.

Theorem 1. *Let $L = 2K$ and $_L\tau_{3p+q}$, $p = 0, 1, \ldots, K-1$, $q = 0, 1, 2$, be defined by (26). Then we have*

$$\sum_{q=0}^{2}\sum_{p=0}^{K-1} {}_L\tau_{3p+q}(\omega)\, \overline{_L\tau_{3p+q}\left(\omega + \frac{2\pi\ell}{L}\right)} = \delta_{\ell,0}, \quad \ell = 0, \ldots, L-1. \tag{27}$$

Proof. Note that for $\ell = 0, \ldots, L-1$

$$\sum_{q=0}^{2}\sum_{p=0}^{K-1} {}_L\tau_{3p+q}(\omega)\, \overline{_L\tau_{3p+q}\left(\omega + \frac{2\pi\ell}{L}\right)}$$

$$= \sum_{q=0}^{2}\sum_{p=0}^{K-1} {}_K\hat{h}_p(2\omega)\, _2\tau_q(\omega)\, \overline{_K\hat{h}_p\left(2\omega + \frac{2\pi\ell}{K}\right)}\, \overline{_2\tau_q\left(\omega + \frac{2\pi\ell}{L}\right)}$$

$$= M_\ell(\omega) \sum_{p=0}^{K-1} {}_K\hat{h}_p(2\omega)\, \overline{_K\hat{h}_p\left(2\omega + \frac{2\pi\ell}{K}\right)},$$

where

$$M_\ell(\omega) = {}_2\tau_0(\omega)\, \overline{_2\tau_0\left(\omega + \frac{2\pi\ell}{L}\right)} + {}_2\tau_1(\omega)\, \overline{_2\tau_1\left(\omega + \frac{2\pi\ell}{L}\right)} + {}_2\tau_2(\omega)\, \overline{_2\tau_2\left(\omega + \frac{2\pi\ell}{L}\right)}.$$

Since $M_0(\omega) = 1$ and $M_K(\omega) = 0$ by (24), and $\sum_{p=0}^{K-1} {}_K\hat{h}_p(2\omega)\, \overline{_K\hat{h}_p(2\omega + (2\pi\ell)/K)} = \delta_{\ell\bmod K, 0}$ by (25), (27) follows. □

Let $_L\hat{\phi}$ be the Fourier transform of the scaling function $_L\phi$ corresponding to the low-pass filter $_L\tau_0$. The functions $_L\psi_{3p+q}$, $0 \leqslant p \leqslant K-1$, $q = 0, 1, 2$, and $(p,q) \neq (0,0)$ defined by

$$_L\hat{\psi}_{3p+q}(\omega) = {}_L\tau_{3p+q}\left(\frac{\omega}{2}\right){}_L\hat{\phi}\left(\frac{\omega}{2}\right)$$

are either symmetric or antisymmetric. Moreover, the system

$$X = \left\{ 2^{L/2} \psi_{3p+q} \left(L^k \cdot - j \right) \colon 0 \leqslant p \leqslant K - 1, \ q = 0, 1, 2, \ (p, q) \neq (0, 0); \ k, j \in \mathbb{Z} \right\}$$

is a tight-frame system of $\mathcal{L}^2(\mathbb{R})$ by Theorem 1 and the unitary extension principle of [19]. We note that for $L = 2K$, this construction gives $3K - 1$ wavelet functions.

Two most commonly used cases in applications are $L = 2$ and $L = 4$. For $L = 4$, the filters associated with the tight-frame system are:

$$_4 m_0 = \frac{1}{4} \left[\frac{1}{2}, 1, 1, 1, \frac{1}{2} \right], \quad _4 m_1 = \frac{\sqrt{2}}{8} [1, 0, 0, 0, -1], \quad _4 m_2 = \frac{1}{4} \left[-\frac{1}{2}, 1, -1, 1, -\frac{1}{2} \right],$$

$$_4 m_3 = \frac{1}{4} \left[\frac{1}{2}, 1, 0, -1, -\frac{1}{2} \right], \quad _4 m_4 = \frac{\sqrt{2}}{8} [1, 0, -2, 0, 1], \quad _4 m_5 = \frac{1}{4} \left[-\frac{1}{2}, 1, 0, -1, \frac{1}{2} \right].$$

We now describe the main ideas of tight-frame algorithm for the high-resolution function reconstruction. The details of implementation will be given in a matrix form in the next two subsections. For simplicity, we discuss the univariate case with $L = 2$. The more general cases can be discussed in the exactly same way except with more complicated notations. We start with the blurring filter without displacement errors. The corresponding tight-frame wavelet filters are already given in (23), and (24) reduces to

$$_2 \tau_0(\omega) \overline{_2 \tau_0(\omega)} + _2 \tau_1(\omega) \overline{_2 \tau_1(\omega)} + _2 \tau_2(\omega) \overline{_2 \tau_2(\omega)} = 1, \tag{28}$$

for a.e. $\omega \in \mathbb{R}$. To simplify the notations, let us just replace $_2 \tau_i$ ($_2 m_i$) by τ_i (m_i), $i = 0, 1, 2$.

Let g be the observed function and f be the true function to recover. Let ϕ be the refinable function corresponding to the low-pass filter m_0, which generated a multiresolution V_n, $n \in \mathbb{Z}$. Then, as the analysis of [2] shows, f can be approximated be a function in V_1, i.e.,

$$f_1 = \sum_{\alpha \in \mathbb{Z}} \langle f, \sqrt{2} \phi(2 \cdot - \alpha) \rangle \sqrt{2} \phi(2 \cdot - \alpha) := \sqrt{2} \sum_{\alpha \in \mathbb{Z}} v(\alpha) \phi(2 \cdot - \alpha). \tag{29}$$

The numbers $v(\alpha)$, $\alpha \in \mathbb{Z}$, are the pixel values of the high-resolution image we are seeking, and they form the discrete representation of f under the basis $\sqrt{2} \phi(2 \cdot - \alpha)$, $\alpha \in \mathbb{Z}$. The given data set $(m_0 * v)(\alpha)$ is the observed high-resolution image. By using the refinability of ϕ, one finds that $m_0 * v$ is the coefficient sequence of the function g represented by $\phi(\cdot - \alpha/2)$, $\alpha \in \mathbb{Z}$, in $V_0(\phi)$. We call this g the *observed function* and it is given by

$$g := \sum_{\alpha \in \mathbb{Z}} (m_0 * v)(\alpha) \phi \left(\cdot - \frac{\alpha}{2} \right).$$

The observed function can be obtained from $m_0 * v$.

When only $m_0 * v$ is given, to recover f_1, one first finds v from $m_0 * v$; then, derives f_1 using the basis $\sqrt{2} \phi(2 \cdot - \alpha)$, $\alpha \in \mathbb{Z}$, as in (29). To recover f_1 from g, we need to restore the wavelet coefficients of f_1 that contain the high frequency components of f_1. Here we provide an iterative algorithm to recover v. At step $(n + 1)$ of the algorithm, it improves the wavelet components of f_1 by updating the wavelet coefficients of the previous step. The algorithm is presented in the Fourier domain where the problem becomes: for a given $\widehat{m_0 * v} = \tau_0 \hat{v}$, one needs to find $\hat{v}$ in order to restore f_1.

Our tight-frame iterative algorithm starts from (28). Suppose that at step n, we have the nth approximation $\hat{v}_n$. Then (28) gives

$$\overline{\tau_0} \tau_0 \hat{v}_n + \overline{\tau_1} \tau_1 \hat{v}_n + \overline{\tau_2} \tau_2 \hat{v}_n = \hat{v}_n.$$

Assume that there is no displacement error. Since $\tau_0 \hat{v} = \widehat{m_0 * v}$ is available, we replace $\tau_0 \hat{v}_n$ by $\widehat{m_0 * v}$ (i.e., $\tau_0 \hat{v}$) to improve the approximation. By this, we define

$$\hat{v}_{n+1} = \overline{\tau_0} \widehat{m_0 * v} + \overline{\tau_1} \tau_1 \hat{v}_n + \overline{\tau_2} \tau_2 \hat{v}_n. \tag{30}$$

It can further be shown via a method similar to that used in [2], that the sequence of functions corresponding to the high-resolution images at each iteration converges to $\hat{v}$ in L^2-norm in the absence of noise. Hence we obtain f_1 by (29).

When g contains noise, then v_n has noise brought in from the previous iteration. To build a denoising procedure into the algorithm, we further decompose the high-frequency components $\tau_1 \hat{v}_n$ and $\tau_2 \hat{v}_n$ via the standard tight-frame wavelet decomposition algorithm. This gives a wavelet frame packet decomposition of v_n. Then, applying a wavelet denoising algorithm to this decomposition and reconstructing $\tau_1 \hat{v}_n$ and $\tau_2 \hat{v}_n$ back via the standard reconstruction algorithm leads to a denoising procedure for $\hat{v}_n$.

For the case with displacement errors, the blurred function g has error from the displacement. In order to take into the consideration the displacement errors and use our algorithm (30), we recall our earlier observation (20) that the coefficients of blurring image g is obtained from v by passing v through the filter $\tau_0 + \sqrt{2}\varepsilon\tau_1$. Noting that

$$\overline{\tau_0(\omega)}\left(\tau_0(\omega) + \sqrt{2}\varepsilon\tau_1(\omega) - \sqrt{2}\varepsilon\tau_1(\omega)\right) + \overline{\tau_1(\omega)}\tau_1(\omega) + \overline{\tau_2(\omega)}\tau_2(\omega) = 1,$$

and the fact that $(\tau_0(\omega) + \sqrt{2}\varepsilon\tau_1(\omega))\hat{v}$ is available, we obtain the following modified algorithm:

$$\hat{v}_{n+1} = \overline{\tau_0}\left((\tau_0 + \sqrt{2}\varepsilon\tau_1)\hat{v} - \sqrt{2}\varepsilon\tau_1\hat{v}_n\right) + \overline{\tau_1}\tau_1\hat{v}_n + \overline{\tau_2}\tau_2\hat{v}_n. \tag{31}$$

Essentially, this algorithm uses $\tau_1 \hat{v}_n$ to estimate the displacement error $\tau_1 \hat{v}$ in $(\tau_0 + \sqrt{2}\varepsilon\tau_1)\hat{v}$, which is the available data. The term $(\tau_0 + \sqrt{2}\varepsilon\tau_1)\hat{v} - \sqrt{2}\varepsilon\tau_1\hat{v}_n$ can be viewed as the approximation of the observed image without displacement errors. By this, we reduce the problem of reconstruction of high-resolution image with the displacement errors to that of the one with no displacement errors. This allows us to use the set of filters derived from the case with no displacement errors. Those filters are symmetric and independent of ε.

4.2. The matrix representation

We now give the matrix representation of the tight-frame system explained in Section 4.1. Both the periodic and the whole-point symmetric boundary conditions are considered. We assume that all the filters $_L m_p$ go from $-K$ to K, where $L = 2K$ and $p = 0, \ldots, 3K - 1$. As we will see in this section, the blurring matrix with displacement errors can be expressed as the sum of the blurring matrix with no displacement errors together with the matrices generated from the filter $_L\tau_1$.

For periodic boundary condition, the matrix representation of $_L\tau_p$ is

$$\mathbf{T}_p^x = \text{Circulant}(\mathbf{a}),$$

where

$$\mathbf{a} = \left[_L m_p(0), \ldots, {}_L m_p(K), 0, \ldots, 0, {}_L m_p(-K), \ldots, {}_L m_p(-1) \right]^{\text{t}}$$

is of dimension M_1 for all $0 \leqslant p < 3K$. The matrix representation of $\overline{_L\tau_p}$ is $(\tilde{\mathbf{T}}_p^x)^{\text{t}}$, which in this case is equal to $(\mathbf{T}_p^x)^{\text{t}}$. Similarly, we can define $\mathbf{T}_p^y$ and $\tilde{\mathbf{T}}_p^y$ and they are equal too.

For the whole-point symmetric boundary condition,

$$\mathbf{T}_p^x = \text{Toeplitz}(\mathbf{a}, \mathbf{b}) + \text{pseudoHankel}(\mathbf{b}, \mathbf{a}),$$

$$\tilde{\mathbf{T}}_p^x = \begin{cases} \mathbf{T}_p^x, & \text{when } p \text{ is even,} \\ \text{Toeplitz}(\mathbf{a}, \mathbf{b}) + \text{pseudoHankel}(-\mathbf{b}, -\mathbf{a}), & \text{when } p \text{ is odd.} \end{cases}$$

Here

$$\mathbf{a} = \big[\,_L m_p(0), \ldots, \,_L m_p(K), 0, \ldots, 0\big]^t \quad \text{and} \quad \mathbf{b} = \big[\,_L m_p(0), \ldots, \,_L m_p(-K), 0, \ldots, 0\big]^t.$$

Similarly, we can define $\mathbf{T}_p^y$ and $\tilde{\mathbf{T}}_p^y$.

For both boundary conditions, Theorem 1 ensures that

$$\sum_{p=0}^{3K-1} \big(\tilde{\mathbf{T}}_p^x\big)^t \mathbf{T}_p^x = \mathbf{I}_{M_1} \quad \text{and} \quad \sum_{p=0}^{3K-1} \big(\tilde{\mathbf{T}}_p^y\big)^t \mathbf{T}_p^y = \mathbf{I}_{M_2}.$$

It leads to

$$\sum_{p,q=0}^{3K-1} \tilde{\mathbf{T}}_{p,q}^t \mathbf{T}_{p,q} = \mathbf{I}_{M_1 \times M_2}, \tag{32}$$

where $\mathbf{T}_{p,q} = \mathbf{T}_q^y \otimes \mathbf{T}_p^x$ and $\tilde{\mathbf{T}}_{p,q} = \tilde{\mathbf{T}}_q^y \otimes \tilde{\mathbf{H}}_p^x$. Obviously, $\mathbf{T}_{0,0} = \tilde{\mathbf{T}}_{0,0} = \mathbf{H}(\mathbf{0}, \mathbf{0})$.

Using our tight-frame system, the blurring matrix with displacement errors can now be expressed as the sum of the blurring matrix with no displacement errors together with the matrices generated from the filter $_L\tau_1$. More precisely, we have

Proposition 1. *Let* $\mathbf{T}_i^x$ *and* $\mathbf{T}_i^y$, $i = 0, 1$, *be the matrix representation of the filters* $_L\tau_0$ *and* $_L\tau_1$ *under either the periodic or the whole-point symmetric boundary conditions. Then for each sensor, the following statements hold*:

$$\mathbf{H}^x\big(\varepsilon_{\ell_1,\ell_2}^x\big) = \mathbf{T}_0^x + \sqrt{2}\varepsilon_{\ell_1,\ell_2}^x \mathbf{T}_1^x, \tag{33}$$

$$\mathbf{H}^y\big(\varepsilon_{\ell_1,\ell_2}^y\big) = \mathbf{T}_0^y + \sqrt{2}\varepsilon_{\ell_1,\ell_2}^y \mathbf{T}_1^y, \tag{34}$$

$$\mathbf{H}_{0,0}\big(\varepsilon_{\ell_1,\ell_2}^x, \varepsilon_{\ell_1,\ell_2}^y\big) = \mathbf{T}_{0,0} + \sqrt{2}\varepsilon_{\ell_1,\ell_2}^x \mathbf{T}_{1,0} + \sqrt{2}\varepsilon_{\ell_1,\ell_2}^y \mathbf{T}_{0,1} + 2\varepsilon_{\ell_1,\ell_2}^x \varepsilon_{\ell_1,\ell_2}^y \mathbf{T}_{1,1}. \tag{35}$$

Proof. The first two equations follow straightforwardly from (20). For (35), we have, by (4), (33), and (34),

$$\mathbf{H}_{0,0}\big(\varepsilon_{\ell_1,\ell_2}^x, \varepsilon_{\ell_1,\ell_2}^y\big) = \mathbf{H}^y\big(\varepsilon_{\ell_1,\ell_2}^y\big) \otimes \mathbf{H}^x\big(\varepsilon_{\ell_1,\ell_2}^x\big) = \big(\mathbf{T}_0^y + \sqrt{2}\varepsilon_{\ell_1,\ell_2}^y \mathbf{T}_1^y\big) \otimes \big(\mathbf{T}_0^x + \sqrt{2}\varepsilon_{\ell_1,\ell_2}^x \mathbf{T}_1^x\big)$$

$$= \mathbf{T}_{0,0} + \sqrt{2}\varepsilon_{\ell_1,\ell_2}^x \mathbf{T}_{1,0} + \sqrt{2}\varepsilon_{\ell_1,\ell_2}^y \mathbf{T}_{0,1} + 2\varepsilon_{\ell_1,\ell_2}^x \varepsilon_{\ell_1,\ell_2}^y \mathbf{T}_{1,1}. \qquad \square$$

By Eq. (6), $\sum_{\ell_1=0}^{L-1} \sum_{\ell_2=0}^{L-1} \mathbf{D}_{\ell_1,\ell_2} = \mathbf{I}_{M_1 \times M_2}$. Therefore, from Proposition 1, we get

Theorem 2. *With the same notations as in Proposition* 1, *we have*

$$\mathbf{H}\big(\boldsymbol{\varepsilon}^x, \boldsymbol{\varepsilon}^y\big) = \mathbf{T}_{0,0} + \sqrt{2}\mathbf{S}\big(\boldsymbol{\varepsilon}^x\big)\mathbf{T}_{1,0} + \sqrt{2}\mathbf{S}\big(\boldsymbol{\varepsilon}^y\big)\mathbf{T}_{0,1} + 2\mathbf{S}\big(\boldsymbol{\varepsilon}^{xy}\big)\mathbf{T}_{1,1}, \tag{36}$$

where $\mathbf{H}\big(\boldsymbol{\varepsilon}^x, \boldsymbol{\varepsilon}^y\big)$ *is given in* (5), $\boldsymbol{\varepsilon}^{xy} = [\varepsilon_{\ell_1,\ell_2}^x \cdot \varepsilon_{\ell_1,\ell_2}^y]_{\ell_1,\ell_2=0}^{L-1}$, *and* $\mathbf{S}(\boldsymbol{\varepsilon}) = \sum_{\ell_1=0}^{L-1} \sum_{\ell_2=0}^{L-1} \varepsilon_{\ell_1,\ell_2} \cdot \mathbf{D}_{\ell_1,\ell_2}$.

Multiplying $\mathbf{f}$ *to both sides of* (36) *leads to*

$$\mathbf{H}\big(\boldsymbol{\varepsilon}^x, \boldsymbol{\varepsilon}^y\big)\mathbf{f} = \mathbf{T}_{0,0}\mathbf{f} + \sqrt{2}\mathbf{S}\big(\boldsymbol{\varepsilon}^x\big)\mathbf{T}_{1,0}\mathbf{f} + \sqrt{2}\mathbf{S}\big(\boldsymbol{\varepsilon}^y\big)\mathbf{T}_{0,1}\mathbf{f} + 2\mathbf{S}\big(\boldsymbol{\varepsilon}^{xy}\big)\mathbf{T}_{1,1}\mathbf{f}.$$

This equation says that the observed high-resolution image $\mathbf{g} = \mathbf{H}(\boldsymbol{\varepsilon}^x, \boldsymbol{\varepsilon}^y)\mathbf{f}$ is the sum of $\mathbf{T}_{0,0}\mathbf{f}$ (which equals to $H(\mathbf{0}, \mathbf{0})\mathbf{f}$, the observed high-resolution image without any displacement errors), and three high-frequency images. Conversely, the observed image in the case with no displacement errors can be represented by the observed images with displacement errors

$$\mathbf{H}(\mathbf{0}, \mathbf{0})\mathbf{f} = \mathbf{T}_{0,0}\mathbf{f} = \mathbf{H}(\boldsymbol{\varepsilon}^x, \boldsymbol{\varepsilon}^y)\mathbf{f} - \left[\sqrt{2}\mathbf{S}(\boldsymbol{\varepsilon}^x)\mathbf{T}_{1,0}\mathbf{f} + \sqrt{2}\mathbf{S}(\boldsymbol{\varepsilon}^y)\mathbf{T}_{0,1}\mathbf{f} + 2\mathbf{S}(\boldsymbol{\varepsilon}^{xy})\mathbf{T}_{1,1}\mathbf{f}\right]. \qquad (37)$$

Thus with the matrices $\mathbf{T}_{1,0}$, $\mathbf{T}_{0,1}$, and $\mathbf{T}_{1,1}$, we can always approximate $\mathbf{H}(\mathbf{0}, \mathbf{0})\mathbf{f}$ once all the displacement errors $\boldsymbol{\varepsilon}^x$ and $\boldsymbol{\varepsilon}^y$ are known. In other words, unlike the work in [3], the tight system we used is fixed and can be used for all displacement errors.

4.3. The algorithm

To obtain our algorithm in matrix form, we follow the discussions at the end of Section 4.1, namely, Eqs. (30) and (31). We first multiply both sides of (32) by $\mathbf{f}$. Recall that $\mathbf{H}(\boldsymbol{\varepsilon}^x, \boldsymbol{\varepsilon}^y)\mathbf{f}$ is the observed high-resolution image $\mathbf{g}$. Hence by (37), we have

$$\mathbf{f} = \tilde{\mathbf{T}}_{0,0}^{\mathrm{t}}\left[\mathbf{g} - \left(\sqrt{2}\mathbf{S}(\boldsymbol{\varepsilon}^x)\mathbf{T}_{1,0} + \sqrt{2}\mathbf{S}(\boldsymbol{\varepsilon}^y)\mathbf{T}_{0,1} + 2\mathbf{S}(\boldsymbol{\varepsilon}^{xy})\mathbf{T}_{1,1}\right)\mathbf{f}\right] + \sum_{\substack{p,q=0 \\ (p,q)\neq(0,0)}}^{3K-1} \tilde{\mathbf{T}}_{p,q}^{\mathrm{t}}\mathbf{T}_{p,q}\mathbf{f}.$$

Thus our tight-frame-based iterative algorithm is

$$\mathbf{f}_{n+1} = \tilde{\mathbf{T}}_{0,0}^{\mathrm{t}}\left[\mathbf{g} - \left(\sqrt{2}\mathbf{S}(\boldsymbol{\varepsilon}^x)\mathbf{T}_{1,0} + \sqrt{2}\mathbf{S}(\boldsymbol{\varepsilon}^y)\mathbf{T}_{0,1} + 2\mathbf{S}(\boldsymbol{\varepsilon}^{xy})\mathbf{T}_{1,1}\right)\mathbf{f}_n\right] + \sum_{\substack{p,q=0 \\ (p,q)\neq(0,0)}}^{3K-1} \tilde{\mathbf{T}}_{p,q}^{\mathrm{t}}\mathbf{T}_{p,q}\mathbf{f}_n.$$

The key step for denoising is to apply thresholding to the wavelet coefficients at each level. For this we define Donoho's thresholding operator [7]. For a given λ, let

$$\mathcal{T}_\lambda\left((x_1, \ldots, x_l, \ldots)^{\mathrm{t}}\right) = \left(t_\lambda(x_1), \ldots, t_\lambda(x_l), \ldots\right)^{\mathrm{t}},$$

where the thresholding function t_λ is either

 (i) $t_\lambda(x) = x\chi_{|x|>\lambda}$, referred to as the *hard threshold*, or
(ii) $t_\lambda(x) = \mathrm{sgn}(x)\max(|x| - \lambda, 0)$, the *soft threshold*.

Altogether, the denoising scheme for two-dimensional image can be simply written as

$$\mathcal{D}(\mathbf{f}) = \left(\tilde{\mathbf{W}}_{0,0}^{\mathrm{t}}\right)^Q(\mathbf{W}_{0,0})^Q\mathbf{f} + \sum_{q=0}^{Q-1}\left(\tilde{\mathbf{W}}_{0,0}^{\mathrm{t}}\right)^q \sum_{\substack{r,s=0 \\ (r,s)\neq(0,0)}}^{2} \tilde{\mathbf{W}}_{r,s}^{\mathrm{t}}\mathcal{T}_\lambda\left(\mathbf{W}_{r,s}\mathbf{W}_{0,0}^q\mathbf{f}\right). \qquad (38)$$

Here the matrices $\mathbf{W}_{r,s}$ and $\tilde{\mathbf{W}}_{r,s}$ correspond to the matrices in (32) with $K = 1$, Q is the number of levels used in the decomposition, and $\mathcal{T}_\lambda$ is the thresholding operator defined in [6,7] with $\lambda = \sigma\sqrt{2\log(M_1 M_2)}$, where σ is the variance of the Gaussian noise in signal $\mathbf{f}$ estimated numerically by the method given in [7]. Below we give the complete algorithm.

Algorithm 1. (1) *Choose an initial guess* $\mathbf{f}_0$.
  (2) *Iterate on n until convergence*

$$\mathbf{f}_{n+1} = (\tilde{\mathbf{T}}_{0,0})^{\mathrm{t}}\big[\mathbf{g} - \big(\sqrt{2}\mathbf{S}(\boldsymbol{\varepsilon}^x)\mathbf{T}_{1,0} + \sqrt{2}\mathbf{S}(\boldsymbol{\varepsilon}^y)\mathbf{T}_{0,1} + 2\mathbf{S}(\boldsymbol{\varepsilon}^{xy})\mathbf{T}_{1,1}\big)\mathbf{f}_n\big]$$
$$+ \sum_{\substack{p,q=0 \\ (p,q)\neq(0,0)}}^{3K-1} (\tilde{\mathbf{T}}_{p,q})^{\mathrm{t}}\mathcal{D}(\mathbf{T}_{p,q}\mathbf{f}_n).$$

Some remarks about the algorithm:

- This algorithm uses the previous iterate to correct the displacement errors of the observed image, as is shown by the terms in the bracket. This allows us to use the same set of filters regardless of the values of the displacement errors. In particular, the symmetric boundary conditions can always be used. This leads to a significant improvement of the reconstructed images as is shown in our numerical simulations in Section 5. The key factor of this algorithm is the special filter design by using the unitary extension principle of [19].
- Since the low-pass filter of our tight frame is given by the blurring kernel with no displacement errors, and since the tight frame is self-dual, images are analyzed and reconstructed with the same set of filters and in the same multiresolution. In contrast, the bi-orthogonal wavelet approach uses different sets of filters in the analysis and the reconstruction and the images are represented in the multiresolution generated by the dual low-pass filter of the blurring kernel. The scaling function corresponding to the dual filter has lower regularity if we require that the dual filter had the same length as the blurring filter. Although it can be avoided by using orthogonal wavelets, there exists no orthonormal wavelet system for the given blurring kernels here. This again shows the flexibilities given by the tight-frame system.
- For the algorithm in [3], a block-Gauss–Seidel-like approach is used, namely, in each iteration, the iteration is carried out on only one sensor while keeping the information on the other sensors fixed. Here, all sensors are updated simultaneously.
- When there are no displacement errors, i.e., $\boldsymbol{\varepsilon}^x = \boldsymbol{\varepsilon}^y = \mathbf{0}$, Step 2 reduces to

$$\mathbf{f}_{n+1} = (\tilde{\mathbf{T}}_{0,0})^{\mathrm{t}}\mathbf{g} + \sum_{\substack{p,q=0 \\ (p,q)\neq(0,0)}}^{3K-1} (\tilde{\mathbf{T}}_{p,q})^{\mathrm{t}}\mathcal{D}(\mathbf{T}_{p,q}\mathbf{f}_n).$$

  In this case, numerical simulations show that the tight-frame method is comparable with the wavelet method.

5. Numerical experiments

In this section, we compare the Tikhonov least-squares method (LS) with the wavelet-based algorithm (WA) (see [2,3]) and the tight-frame-based algorithm (TF) (i.e., Algorithm 1 above). We evaluate the

Fig. 3. Original "boat" image (left); original "bridge" image (right).

methods using the relative error (RE) and the peak signal-to-noise ratio (PSNR) which compare the reconstructed image $\mathbf{f}_c$ with the original image $\mathbf{f}$. They are defined by

$$\text{RE} = \frac{\|\mathbf{f} - \mathbf{f}_c\|_2}{\|\mathbf{f}\|_2} \quad \text{and} \quad \text{PSNR} = 10 \log_{10} \frac{255^2 M_1 M_2}{\|\mathbf{f} - \mathbf{f}_c\|_2^2},$$

where the size of the restored images is $M_1 \times M_2 = 256 \times 256$. We use the "bridge" and "boat" images of size 260×260 as the original images in our numerical tests, see Fig. 3. For both WA and TF, we use the hard thresholding operator $\mathcal{T}_\lambda$ and $Q = 1$ in (38).

5.1. The case without displacement errors

In this case, the high-resolution image reconstruction is equivalent to deblurring a blurred image, which is the convolution of the original image with the two-dimensional filter $_L\tau_0^t {}_L\tau_0$. For LS, the regularization functional $\mathbf{R}$ is chosen to be the identity and we use the half-point boundary condition in formulating the blurring matrix $\mathbf{H}(\mathbf{0}, \mathbf{0})$. The resulting system can be solved by three two-dimensional fast cosine transforms [16]. For both WA and TF, the whole-point boundary condition is used to formulate the blurring matrix $\mathbf{H}(\mathbf{0}, \mathbf{0})$. The iterate process stops when the highest PSNR is achieved. Tables 1 and 2 show that WA and TF give a significantly improvement over LS for the "boat" image and a comparable result for the "bridge" image. The restored images are shown in Fig. 4 for the 4×4 sensor array at SNR of 30 dB.

Table 1
The results for the 2×2 sensor array

Image	SNR	LS			WA			TF		
		PSNR	RE	β^*	PSNR	RE	Ite	PSNR	RE	Ite
Boat	20	30.62	0.0544	0.02425	33.51	0.0390	10	33.87	0.0374	38
	30	32.58	0.0434	0.01698	35.20	0.0321	18	35.41	0.0313	62
	40	33.91	0.0372	0.01335	36.17	0.0287	24	36.27	0.0284	84
Bridge	20	28.49	0.0832	0.01981	29.05	0.0780	16	28.94	0.0791	81
	30	29.55	0.0736	0.01214	29.57	0.0735	26	29.31	0.0758	107
	40	30.22	0.0682	0.00850	29.78	0.0717	32	29.44	0.0746	97

Table 2
The results for the 4 × 4 sensor array

Image	SNR	LS			WA			TF		
		PSNR	RE	β^*	PSNR	RE	Ite	PSNR	RE	Ite
Boat	20	28.44	0.0699	0.01918	29.80	0.0597	33	29.49	0.0619	70
	30	29.46	0.0621	0.01233	30.86	0.0529	59	30.58	0.0546	142
	40	30.16	0.0573	0.00890	31.57	0.0487	93	31.26	0.0505	177
Bridge	20	25.39	0.1189	0.01266	25.76	0.1139	75	25.76	0.1140	140
	30	26.03	0.1105	0.00695	26.08	0.1098	118	26.15	0.1090	180
	40	26.48	0.1049	0.00451	26.19	0.1084	143	26.28	0.1074	180

Table 3
The results with displacement error for the 2 × 2 and 4 × 4 sensor arrays with WA and TF

Image	SNR	2 × 2 sensor array						4 × 4 sensor array					
		WA			TF			WA			TF		
		PSNR	RE	Iter	PSNR	RE	Ite	PSNR	RE	Iter	PSNR	RE	Iter
Boat	20	30.45	0.0559	1	33.87	0.0374	33	27.16	0.0810	2	29.35	0.0629	66
	30	30.80	0.05324	2	35.41	0.0313	56	27.20	0.0806	2	30.38	0.0558	130
	40	30.85	0.05234	2	36.26	0.0284	74	27.21	0.0805	2	31.06	0.0517	180
Bridge	20	27.66	0.0916	4	28.89	0.0795	65	23.99	0.1398	4	25.66	0.1152	134
	30	27.92	0.0889	5	29.22	0.0765	68	24.01	0.1395	4	26.05	0.1102	180
	40	28.00	0.0881	4	29.37	0.0752	88	24.01	0.1393	4	26.19	0.1084	180

5.2. The case with displacement error

For the 2 × 2 sensor array, the displacement errors

$$\boldsymbol{\varepsilon}^x = \begin{bmatrix} -0.2810 & 0.1789 \\ -0.4530 & 0.1793 \end{bmatrix}, \qquad \boldsymbol{\varepsilon}^y = \begin{bmatrix} 0.4347 & 0.0194 \\ -0.1165 & 0.3310 \end{bmatrix}$$

are used in our simulation. For the 4 × 4 sensor array, we use

$$\boldsymbol{\varepsilon}^x = \begin{bmatrix} -0.2810 & 0.4347 & -0.4654 & -0.4923 \\ -0.4530 & -0.1165 & -0.4465 & -0.1166 \\ 0.1789 & 0.0194 & 0.0297 & -0.4332 \\ 0.1793 & 0.3310 & 0.1711 & -0.0825 \end{bmatrix},$$

$$\boldsymbol{\varepsilon}^y = \begin{bmatrix} 0.1868 & 0.0269 & 0.2012 & -0.4525 \\ 0.0890 & -0.4080 & 0.4103 & 0.2361 \\ 0.4304 & 0.1539 & 0.2622 & -0.1718 \\ 0.3462 & -0.0840 & -0.2375 & 0.1326 \end{bmatrix}.$$

The numerical results are shown in Table 3, where the maximum number of iteration is 180. We remark that the tight-frame-based algorithm is not sensitive to $\boldsymbol{\varepsilon}^x$ or $\boldsymbol{\varepsilon}^y$. The reconstructed "boat" and "bridge" images are shown in Figs. 5 and 6, respectively.

Fig. 4. 4 × 4 sensor array without displacement error at SNR of 30 dB. The images (from top to bottom) are: observed high-resolution image, results with LS, WA, and TF, respectively.

Fig. 5. 4 × 4 sensor array with displacement error at SNR of 30 dB for "boat" image. A low-resolution image from the (0, 0) sensor (top-left); observed high-resolution images (top-right); reconstructed images with WA (bottom-left); and TF (bottom-right).

Fig. 6. 4 × 4 sensor array with displacement error at SNR of 30 dB for "bridge" image. A low-resolution image from the (0, 0) sensor (top-left); observed high-resolution images (top-right); reconstructed images with WA (bottom-left); and TF (bottom-right).

References

[1] N. Bose, K. Boo, High-resolution image reconstruction with multisensors, Int. J. Imaging Syst. Technol. 9 (1998) 294–304.

[2] R. Chan, T. Chan, L. Shen, Z. Shen, Wavelet algorithms for high-resolution image reconstruction, SIAM J. Sci. Comput. 24 (4) (2003) 1408–1432.

[3] R. Chan, T. Chan, L. Shen, Z. Shen, Wavelet deblurring algorithms for spatially varying blur from high-resolution image reconstruction, Linear Algebra Appl. 366 (2003) 139–155.

[4] I. Daubechies, Ten Lectures on Wavelets, in: CBMS Conf. Ser. Appl. Math., vol. 61, SIAM, Philadelphia, 1992.

[5] C. de Boor, R. DeVore, A. Ron, On the construction of multivariate (pre)-wavelets, Constr. Approx. 9 (1993) 123–166.

[6] D. Donoho, De-noising by soft-thresholding, IEEE Trans. Inform. Theory 41 (1995) 613–627.

[7] D. Donoho, I. Johnstone, Ideal spatial adaptation by wavelet shrinkage, Biometrika 81 (1994) 425–455.

[8] M. Elad, A. Feuer, Restoration of a single superresolution image from several blurred, noisy and undersampled measured images, IEEE Trans. Image Process. 6 (Dec. 1997) 1646–1658.

[9] M. Elad, A. Feuer, Superresolution restoration of an image sequence: adaptive filtering approach, IEEE Trans. Image Process. 8 (3) (Mar. 1999) 387–395.

[10] J.C. Gillete, T.M. Stadtmiller, R.C. Hardie, Aliasing reduction in starting infrared images utilizing subpixel techniques, Optical Engrg. 34 (11) (Nov. 1995) 3130.

[11] P. Heller, Rank M wavelets with N vanishing moments, SIAM J. Matrix Anal. Appl. 16 (1995) 502–519.

[12] T. Huang, R. Tsay, Multiple frame image restoration and registration, in: T.S. Huang (Ed.), Advances in Computer Vision and Image Processing, vol. 1, JAI, Greenwich, CT, 1984, pp. 317–339.

[13] R. Jia, Z. Shen, Multiresolution and wavelets, Proc. Edinburgh Math. Soc. 37 (1994) 271–300.

[14] W. Lawton, S. Lee, Z. Shen, An algorithm for matrix extension and wavelet construction, Math. Comput. 65 (1996) 723–737.

[15] M. Ng, R. Chan, T. Chan, A. Yip, Cosine transform preconditioners for high resolution image reconstruction, Linear Algebra Appl. 316 (2000) 89–104.

[16] M. Ng, R. Chan, W. Tang, A fast algorithm for deblurring models with Neumann boundary conditions, SIAM J. Sci. Comput. 21 (2000) 851–866.

[17] M.K. Ng, N. Bose, Analysis of displacement errors in high-resolution image reconstruction with multisensors, IEEE Trans. Circuits Systems I Fund. Theory Appl. 49 (6) (2002) 806–813.

[18] A. Patti, M. Sezan, A. Tekalp, Superresolution video reconstruction with arbitrary sampling lattices and nonzero aperture time, IEEE Trans. Image Process. 6 (Aug. 1997) 1064–1076.

[19] A. Ron, Z. Shen, Affine system in $L_2(\mathbb{R}^d)$: the analysis of the analysis operator, J. Funct. Anal. 148 (1997) 408–447.

[20] R. Schultz, R. Stevenson, Extraction of high-resolution frames from video sequences, IEEE Trans. Image Process. 5 (June 1996) 996–1011.

[21] L. Shen, Q. Sun, Bi-orthogonal wavelet system for high-resolution image reconstruction, IEEE Trans. Signal Process. (2003), submitted for publication.

[22] Z. Shen, Extension of matrices with Laurent polynomial entries, in: Proceedings of the 15th IMACS World Congress on Scientific Computation Modeling and Applied Mathematics, vol. 1, 1997, pp. 57–61.